Supplementary Information

Forecasting the Flame: Simulating Future Wildfire Regimes in the Northeast Mediterranean

Bikem Ekberzade[1*]

[1]Istanbul Technical University, Eurasia Institute of Earth Sciences

*Corresponding author: Bikem Ekberzade (ekberzade19@itu.edu.tr)

Table S1. List of the five CMIP6 Global Climate Model (GCM) datasets used for future projections under SSP5-8.5. Bias correction was performed using Quantile Delta Mapping (QDM, explained in methodology†). Raw trend (T_R), Corrected trend (T_C) and Relative difference (computed as Relative Difference (%) = ((Corrected Trend - Raw Trend) / Raw Trend) * 100) are listed for each variable: precipitation (pr), relative humidity (rh), shortwave solar radiation (ssrd), minimum, maximum and mean temperatures (T_{min}, T_{max}, T_{mean}), and wind speed (wind). For temperature variables, which were bias-corrected on a month-by-month basis to preserve the diurnal temperature range, the T_R and T_C values represent the annualized aggregate trend.

Model Name	Resolution (km)	Variant Label	Variable	T_R	T_C	Relative Difference
EC-Earth 3p-HR ** (Haarsma et al. 2020)	50	r3i1p2f1	pr	0.9154	0.9686	5.82
			rh	0.9532	0.9382	-1.57
			ssrd	1.0107	1.0101	-0.06
			T_{mean}	1.0194	1.021	0.16
			T_{max}	1.0193	1.021	0.17
			T_{min}	1.0198	1.0213	0.15
			wind	0.9838	0.992	0.83
CMCC-ESM2 (Lovato et al. 2022)	100	r1i1p1f1	pr	0.9235	0.982	6.33
			rh	0.9488	0.9402	-0.91
			ssrd	1.0331	1.0289	-0.41
			T_{mean}	1.0198	1.0209	0.11

			T_{max}	1.0207	1.0209	0.02
			T_{min}	1.0194	1.0213	0.19
			wind	0.9742	0.9875	1.37
INM-CM5 (Volodin and Gritsun 2018)	100	r1i1p1f1	pr	0.9589	0.9945	3.71
			rh	0.9431	0.9452	0.22
			ssrd	1.0167	1.0165	-0.02
			T_{mean}	1.0133	1.0141	0.08
			T_{max}	1.0138	1.0152	0.14
			T_{min}	1.0126	1.0134	0.08
			wind	0.9695	0.9718	0.24
MPI-ESM1-2-HR (Gutjahr et al. 2019)	100	r1i1p1f1	pr	0.8869	1.0303	16.17
			rh	0.9373	0.9428	0.59
			ssrd	1.0003	1.0073	0.70
			T_{mean}	1.0142	1.0142	0.00
			T_{max}	1.0142	1.014	-0.02

			T_{min}	1.0147	1.0147	0.00
			wind	0.9599	0.9741	1.48
NorESM2-MM (Seland et al. 2020)	100	r1i1p1f1	pr	0.86	0.9684	12.60
			rh	0.9491	0.9372	-1.25
			ssrd	1.0262	1.0241	-0.20
			T_{mean}	1.0159	1.0169	0.10
			T_{max}	1.0168	1.0178	0.10
			T_{min}	1.0151	1.0161	0.10
			wind	0.975	0.9803	0.54

† As shown in Table S1, the QDM bias correction successfully preserves the raw GCM trends for the majority of meteorological variables, with relative differences largely remaining below 2%. However, precipitation exhibits higher relative differences, particularly for the MPI-ESM1-2-HR (16.17%) and NorESM2-MM (12.60%) models. These larger deviations are a recognized characteristic of bias-correcting episodic, zero-bounded variables. Unlike temperature, which relies on additive (absolute) shift corrections, precipitation requires multiplicative (relative) scaling to prevent the generation of physically impossible negative values. Because precipitation distributions often contain many dry days and non-normal extremes, correcting the frequency of wet days and the intensity of heavy rainfall events can slightly alter the aggregate trend. Furthermore, when the raw absolute trend is a very small number, even minor adjustments made during the quantile mapping process translate into larger percentage-based relative differences. Therefore, these deviations reflect the mathematical constraints of preserving multiplicative trends in highly variable precipitation data, rather than a failure of the QDM algorithm.

References:

Gutjahr O, Putrasahan D, Lohmann K, Jungclaus JH, von Storch J-S, Brüggemann N, Haak H, and Stössel A (2019) Max Planck Institute Earth System Model (MPI-ESM1.2) for the High-Resolution Model Intercomparison Project (HighResMIP). Geosci. Model Dev., 12:3241–3281. https://doi.org/10.5194/gmd-12-3241-2019

Haarsma R, Acosta M, Bakhshi R, Bretonnière P-A, Caron L-P, Castrillo M, Corti S, Davini P, Exarchou E, Fabiano F, Fladrich U, Fuentes Franco R, García-Serrano J, von Hardenberg J, Koenigk T, Levine X, Meccia VL, van Noije T, van den Oord G, Palmeiro FM, Rodrigo M, Ruprich-Robert Y, Le Sager P, Tourigny E, Wang S, van Weele M, and Wyser K (2020) HighResMIP versions of EC-Earth: EC-Earth3P and EC-Earth3P-HR – description, model computational performance and basic validation. Geosci. Model Dev., 13:3507–3527. https://doi.org/10.5194/gmd-13-3507-2020

Seland Ø, Bentsen M, Olivié D, Toniazzo T, Gjermundsen A, Graff LS, Debernard JB, Gupta AK, He Y-C, Kirkevåg A, Schwinger J, Tjiputra J, Aas KS, Bethke I, Fan Y, Griesfeller J, Grini A, Guo C, Ilicak M, Karset IHH, Landgren O, Liakka J, Moseid KO, Nummelin A, Spensberger C, Tang H, Zhang Z, Heinze C, Iversen T, and Schulz M (2020) Overview of the Norwegian Earth System Model (NorESM2) and key climate response of CMIP6 DECK, historical, and scenario simulations. Geosci. Model Dev., 13:6165–6200. https://doi.org/10.5194/gmd-13-6165-2020

Institute for Numerical Mathematics (2020) WCRP CMIP6: Institute for Numerical Mathematics (INM) INM-CM5-0 model output for the "1pctCO2" experiment. Centre for Environmental Data Analysis. https://catalogue.ceda.ac.uk/uuid/5b50fd3fe7b74a64be91fb7ebb8c21a9 Accessed 12 Dec 2022.

Lovato T, Peano D, Butenschön M, Materia S, Iovino D, Scoccimarro E, et al. (2022) CMIP6 simulations with the CMCC Earth System Model (CMCC-ESM2). Journal of Advances in Modeling Earth Systems, 14, e2021MS002814. https://doi.org/10.1029/2021MS002814

Volodin E, Gritsun A (2018) Simulation of observed climate changes in 1850–2014 with climate model INM-CM5, Earth Syst. Dynam., 9, 1235–1242. https://doi.org/10.5194/esd-9-1235-2018

**** Sample plots for EC-Earth 3p-HR showing the result of QDM bias correction for each variable:** To visually confirm the preservation of the historical climatology and distributions, sample plots of the QDM bias correction results are provided below (Figures S1-S7).

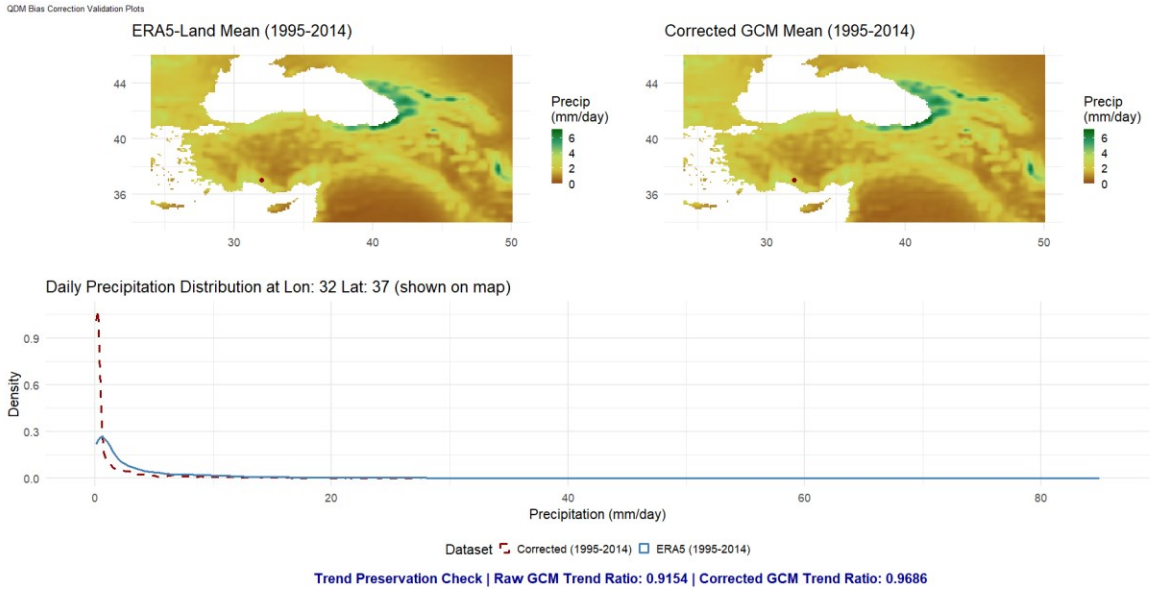

Figure S1. Results for QDM bias correction on EC-Earth precipitation. Maps show mean for reference period (1995-2014) which was used in bias correction. Red dot on the maps marks the sample grid cell for which daily precipitation distribution was plotted (below).

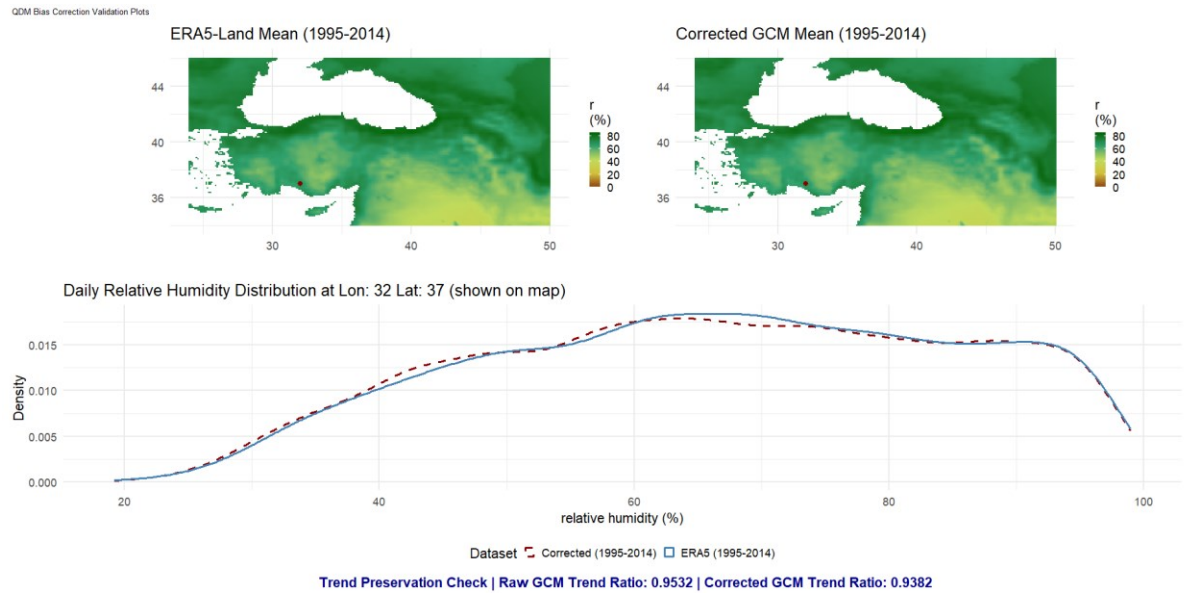

Figure S2. Results for QDM bias correction on EC-Earth relative humidity. Maps show mean for reference period (1995-2014) which was used in bias correction. Red dot on the maps marks the sample grid cell for which daily relative humidity distribution was plotted (below).

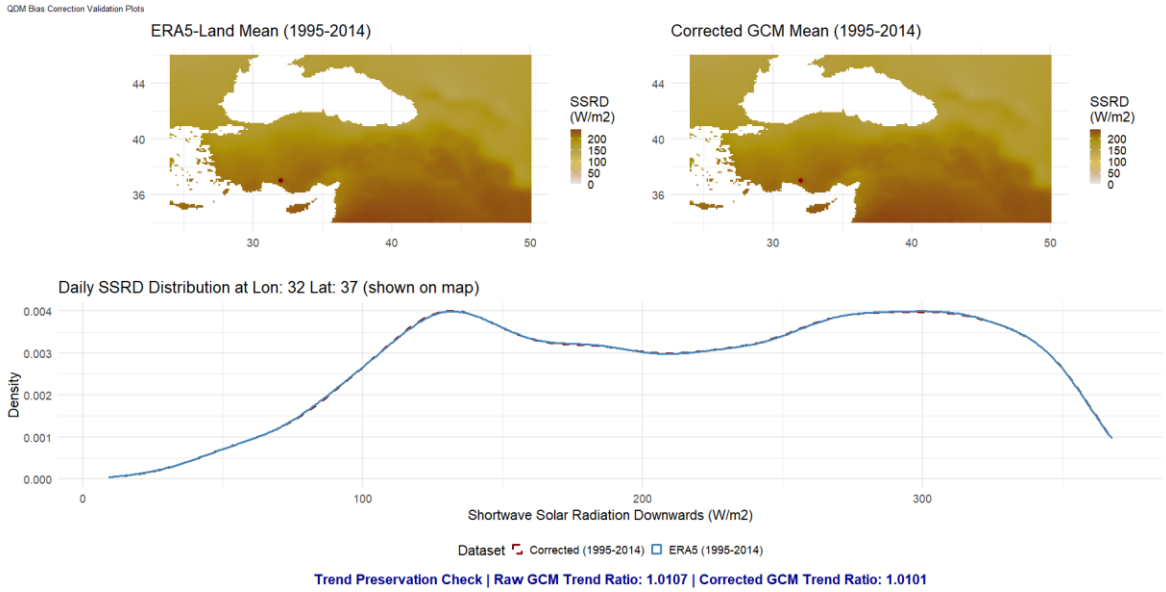

Figure S3. Results for QDM bias correction on EC-Earth shortwave solar radiation downwards. Maps show mean for reference period (1995-2014) which was used in bias correction. Red dot on the maps marks the sample grid cell for which daily shortwave solar radiation distribution was plotted (below).

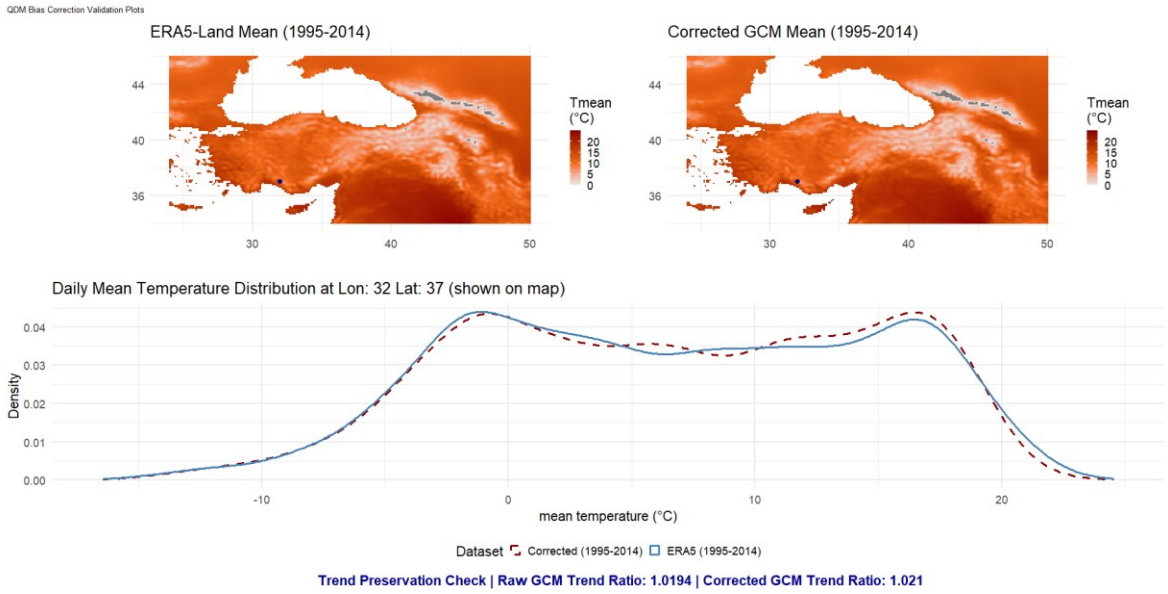

Figure S4. Results for QDM bias correction on EC-Earth mean temperature. Maps show mean for reference period (1995-2014) which was used in bias correction. Blue dot on the maps marks the sample grid cell for which daily mean temperature distribution was plotted (below).

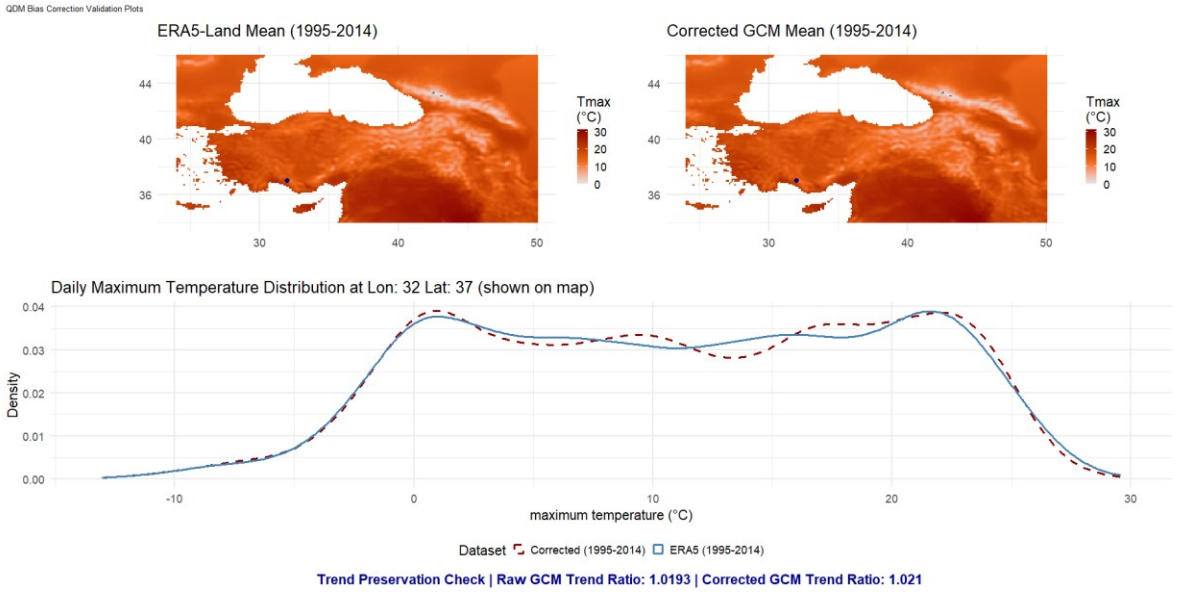

Figure S5. Results for QDM bias correction on EC-Earth maximum temperature. Maps show mean for reference period (1995-2014) which was used in bias correction. Blue dot on the maps marks the sample grid cell for which daily maximum temperature distribution was plotted (below).

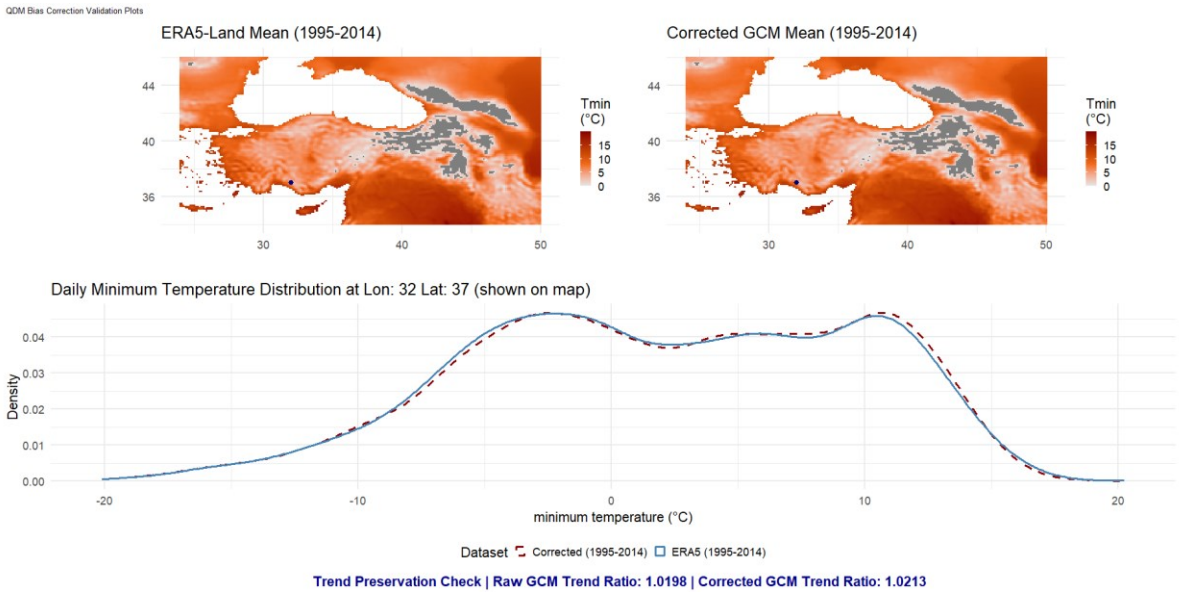

Figure S6. Results for QDM bias correction on EC-Earth minimum temperature. Maps show mean for reference period (1995-2014) which was used in bias correction. Blue dot on the maps marks the sample grid cell for which daily minimum temperature distribution was plotted (below).

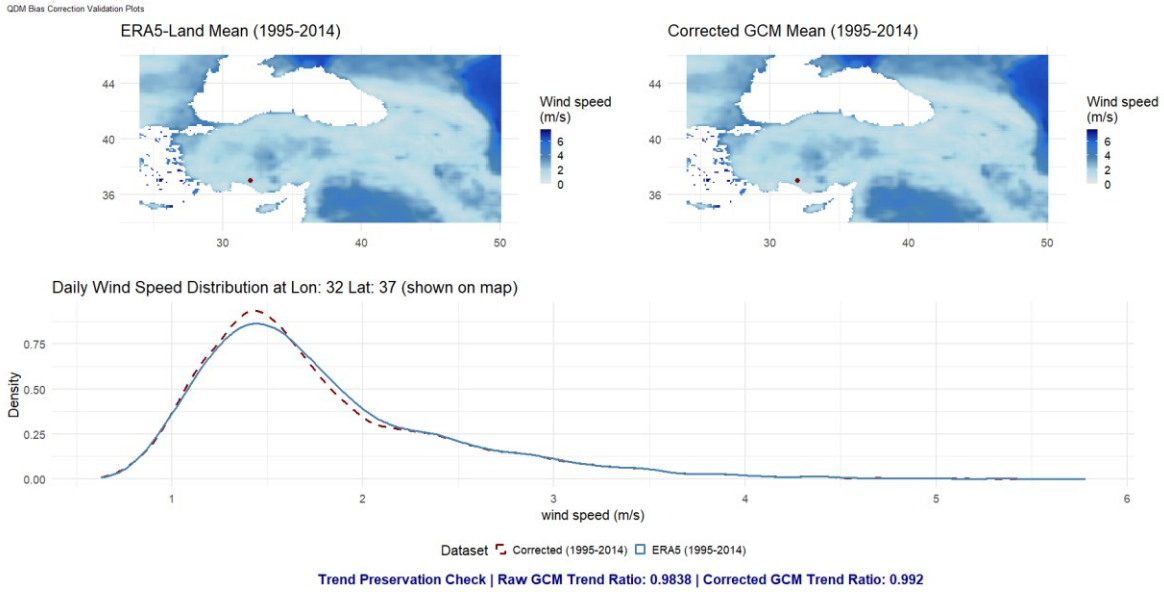

Figure S7. Results for QDM bias correction on EC-Earth wind speed. Maps show mean for reference period (1995-2014) which was used in bias correction. Red dot on the maps marks the sample grid cell for which daily wind speed distribution was plotted (below).

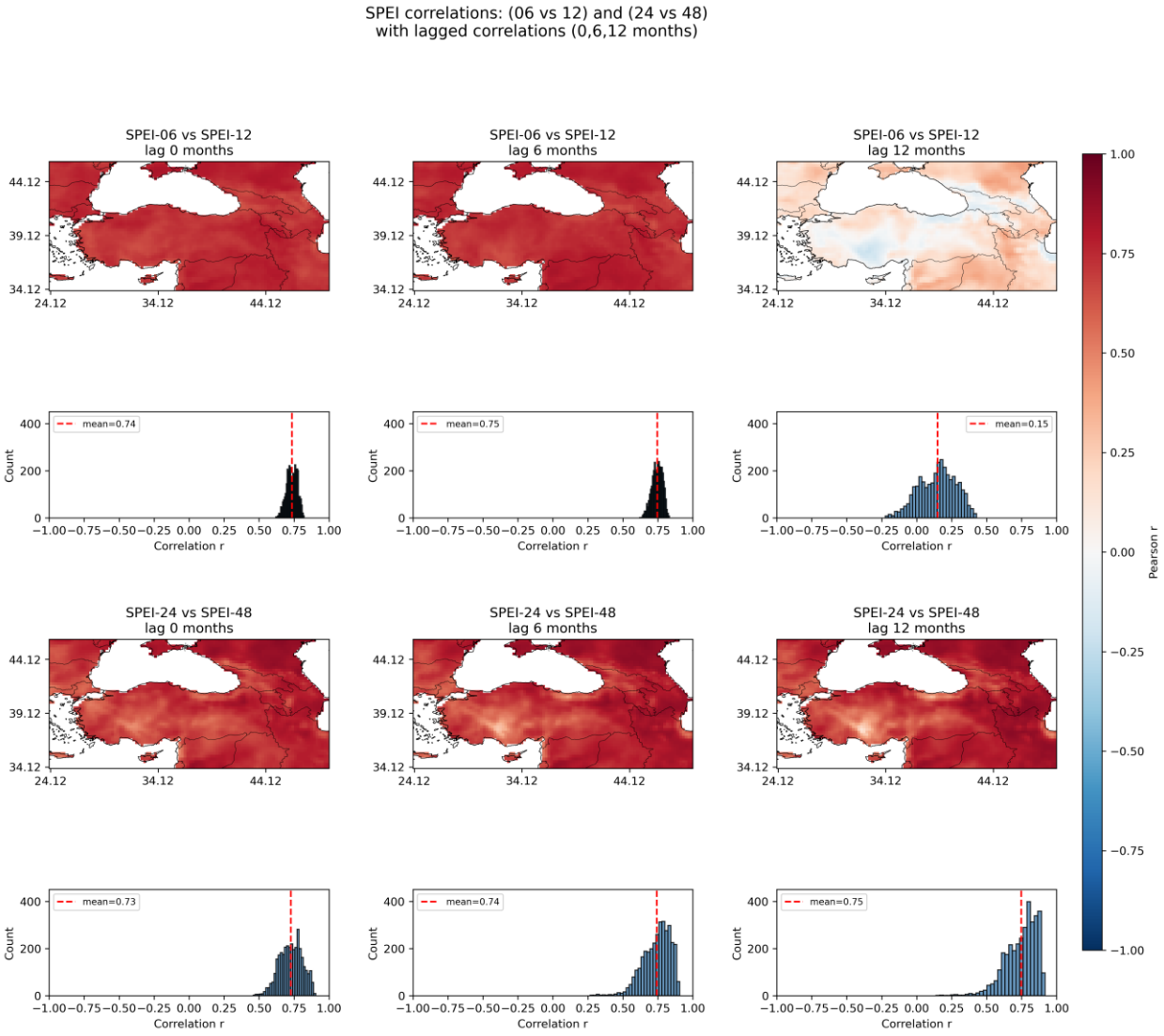

Figure S8: Assessment of drought memory decay across short- and long-term accumulation periods. Maps and histograms display the Pearson correlations between differing Standardized Precipitation Evapotranspiration Index (SPEI) timescales. The top row (SPEI-06 vs SPEI-12) illustrates a significant decay in correlation strength at a 12-month lag (mean r = 0.15), indicating limited persistence. In contrast, the bottom row (SPEI-24 vs. SPEI-48) demonstrates robust long-term memory, retaining high correlation values (mean r ~0.75) even after a 12-month lag.

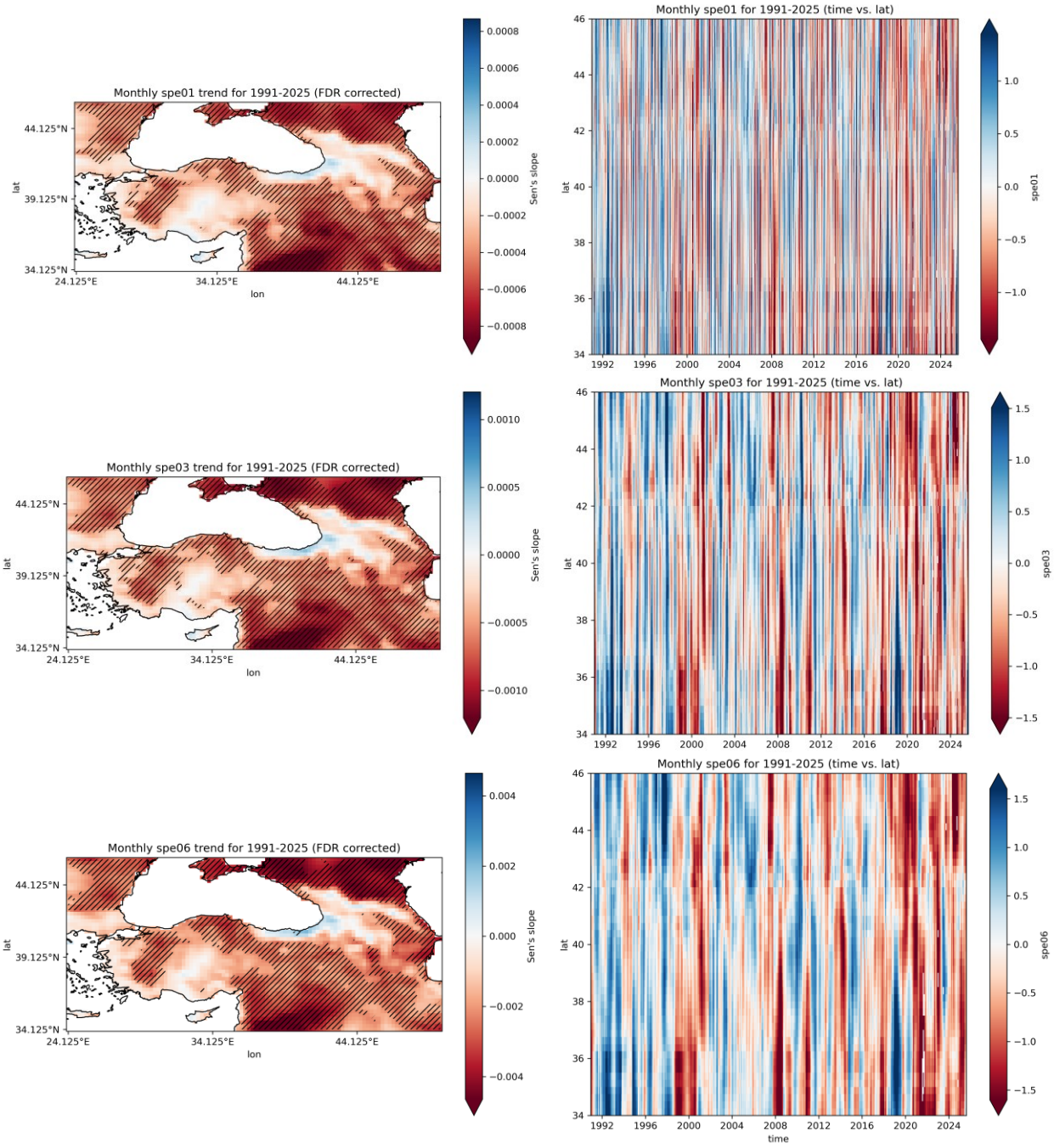

Figure S9: The Standardized Precipitation Evapotranspiration Index (SPEI01-06). Spatial distribution of drought at different monthly intervals (1, 3, 6) using Sen's slope estimator. Hatched areas in maps (left) indicate statistically significant trends ($p < 0.05$), while Hovmöller diagrams (right; Time vs Latitude) illustrate the decisive shift from wetter (blue) to dryer (red) conditions.

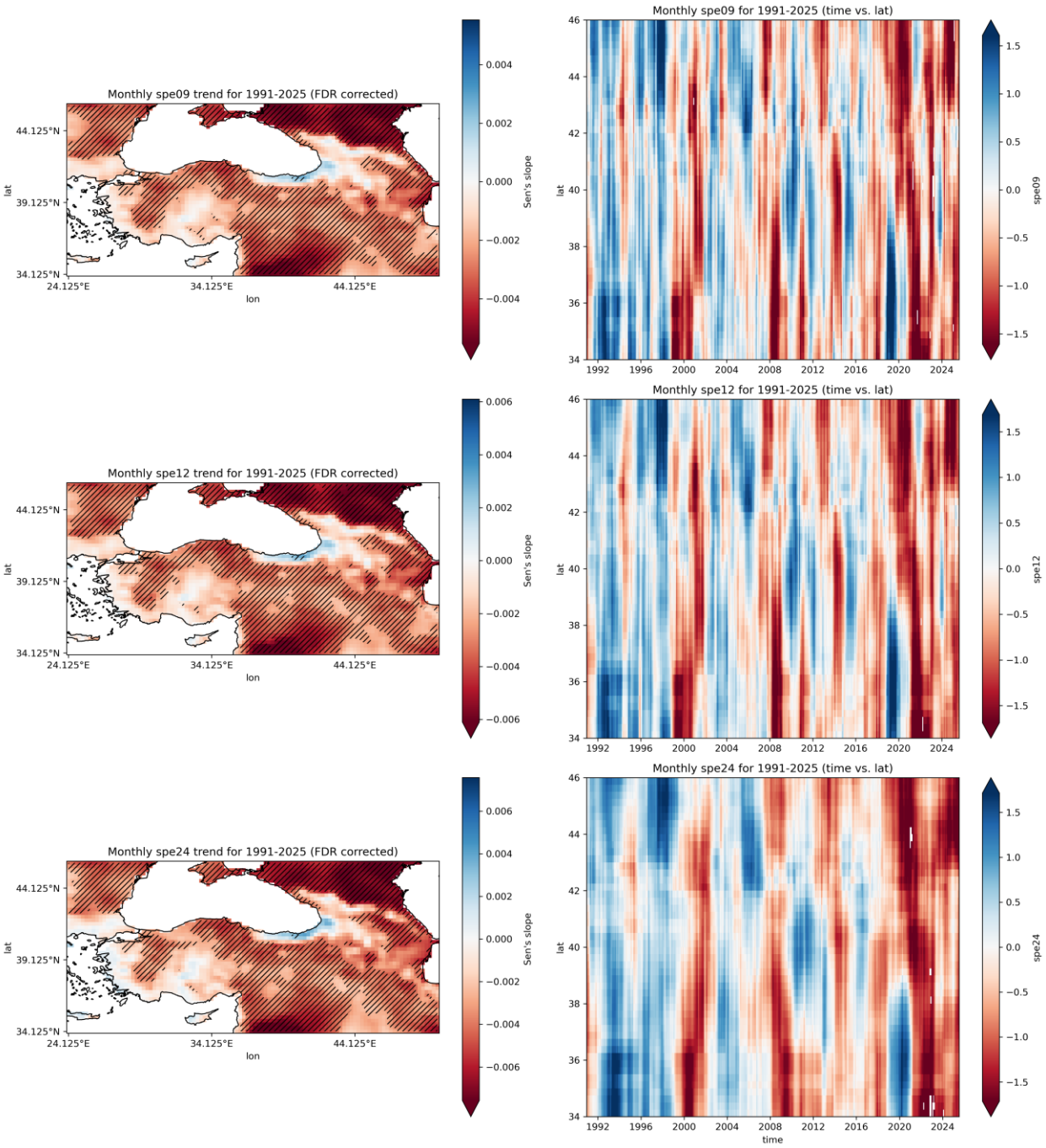

Figure S10. The Standardized Precipitation Evapotranspiration Index (SPEI09-24). Spatial distribution of drought at different monthly intervals (9, 12, 24) using Sen's slope estimator. Hatched areas in maps (left) indicate statistically significant trends ($p < 0.05$), while Hovmöller diagrams (right; Time vs Latitude) illustrate the decisive shift from wetter (blue) to dryer (red) conditions. Note the latitudinal spread of dry conditions, indicating the drought signal becoming persistent across the study domain after 2020.